Evidence suggesting frazil ice crystal formation at the front of Hisinger Glacier in Dickson Fjord, Northeast Greenland

Fleur Rooijakkers [1], Ebbe Poulsen [2], Eugenio Ruiz-Castillo [2], and Søren Rysgaard [2]

[1]Department of Applied Sciences, Delft University of Technology, Delft, 2600 AA, the Netherlands
[2]Arctic Research Centre, Department of Biology, Aarhus University Aarhus, DK-8000, Denmark

Correspondence: Fleur Rooijakkers (fleur.rooijakkers@hotmail.com)

Abstract. Glacier retreat and mass loss in Northeast Greenland have profound implications for global sea-level rise, making it crucial to understand the complex dynamics of glacier-ocean interactions. Currently, our knowledge of Northeast Greenland glacial fjords is limited, and the processes occurring directly in front of these glaciers, particularly the fate of subglacial meltwater, remain insufficiently understood. In this study, conducted in Dickson Fjord, Northeast Greenland in August 2022,

5 hydrographic and stable isotope measurements at various depths and fjord locations have been carried out, starting from the glacier terminus. Employing a drone-deployed ocean profiler, we obtained salinity and temperature profiles as close as 20 m from the glacier terminus. Interestingly, the terminus is primarily in contact with a cold Polar Water layer, leading to unique freshwater dynamics. Our findings provide compelling evidence that subglacial meltwater undergoes freezing upon encountering the cold, saline fjord waters at the terminus. The buoyant ice crystals (frazil) formed during this refreezing process

10 ascend to the surface, where they encounter positive ocean temperatures, causing the ice crystals to melt. Consequently, we observe a depletion in the δ^{18}O and δ^2H isotopic signals around the ice melting line for freshwater (0 °C), separated from the depletion caused by surface runoff. Additionally, an increase in ocean temperatures is found near the glacier, which can be attributed to the latent heat released during the ice crystal formation described.

1 Introduction

15 Climate change has triggered an accelerated mass loss from the Greenland ice sheet (GIS), substantially contributing to the rise in global sea levels and Arctic Ocean freshening (Velicogna (2009); Straneo and Cenedese (2015)). A significant portion of GIS mass loss (88% (Mortensen et al. (2020))) can be attributed to melting at the front of marine-terminating glaciers (Straneo et al. (2012)). While the focus has typically been on marine-terminating glaciers in West and Southeast Greenland, the glaciers in Northeast Greenland are less studied, even though they are also experiencing significant ice loss through dynamic

20 thinning (Arndt et al. (2015); Khan et al. (2014)). Along with the increase in surface melt, the interaction of deeper warmer Atlantic Water masses with the glacier terminus has been found to increase submarine melting (Straneo et al. (2012); Zhao (2022); Holland et al. (2008)). However, the scarcity of measurements at the ice-ocean interface, due to the difficulty and danger involved in obtaining such data, limits our understanding of the complex meltwater dynamics at the ice-ocean boundary (Mortensen et al. (2020); Straneo and Cenedese (2015); Straneo et al. (2012); Zhao (2022)).

25   Here, we present data from a fjord survey conducted in August 2022 within Dickson Fjord, located in Northeast Greenland at 72 °N (Fig. 1). Dickson Fjord is part of the intricate Kempes fjord system, which includes Röhss Fjord and Rhedin Fjord. This study aims to address the existing knowledge gap concerning the fate of glacial meltwater and the dynamics between glacier and ocean in the understudied Northeast Greenland where cold Polar Waters predominate. Salinity and temperature profiles were obtained as close as 20 m from the glacier terminus by deploying an ocean profiler via drone, making this dataset
30   unique in both its geographic location and its measurements in close proximity to the glacier front.

Firstly, we provide background information on the oceanic conditions and glaciers in the study area. Following this, the subsequent sections focus on analysing salinity, temperature transects, and isotopic profiles to understand in-fjord water layer distribution, spatial variation, and the dispersal patterns of in-fjord meltwater. Subsequently, calculations have been performed to interpret and explain the phenomena observed in the dataset.

35   This study highlights the importance of considering the complex vertical and horizontal movements and transformations of glacial meltwater in understanding the freshwater dynamics in glacial fjords. These findings contribute to ongoing efforts to accurately model and predict the impacts of glacial meltwater on the coastal region, ecosystem dynamics, and global sea-level rise.

2   Theory and method

40   2.1   Study location and instrumentation

The main dataset used in this study consists of measurements conducted in Dickson Fjord, Northeast Greenland in August 2022 (Fig. 1).
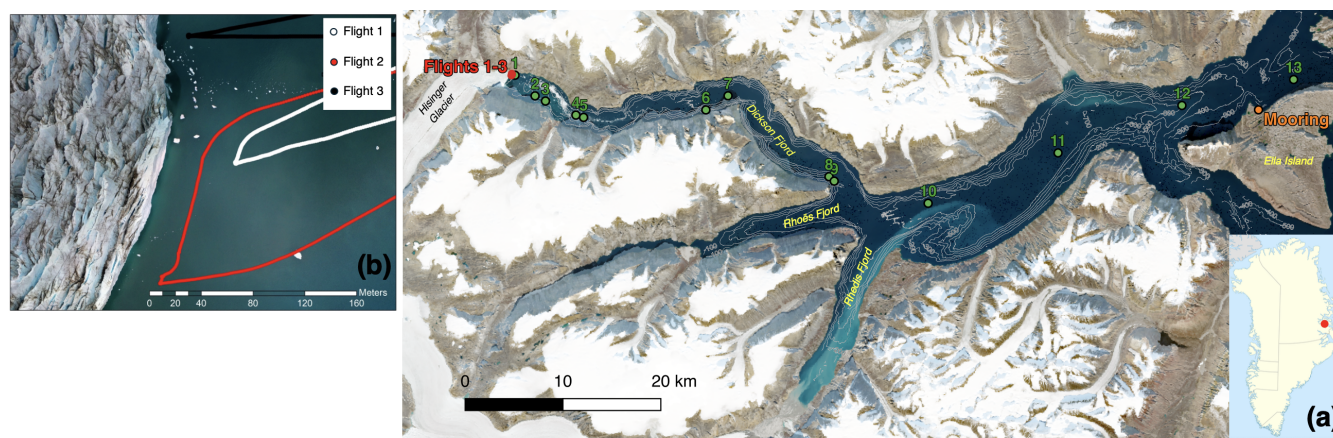
Figure 1. (a) Map of locations of measurement stations used in this study, including high-resolution 100 m bathymetry contour lines. The green dots indicate the locations where the CTD was deployed. At stations 1, 5, 7, 9 and 13, water samples were collected for stable isotope analysis alongside the CTD deployment. The map was generated using Modified Copernicus Sentinel data August 2022/Sentinel Hub. (b) A close-up image of the flight trajectories of the drone-deployed CTD, courtesy of Jeffrey Taylor Kerby.

Dickson Fjord is the northwesternmost fjord in the Kong Oscar fjord system, located in Northeast Greenland at 72 degrees North. This intricate system, including Dickson Fjord, Röhss Fjord, and Rhedin Fjord, forms the Kempes fjord system. At Dickson Fjord's head lies the terminus of the Hisinger glacier, a marine-terminating glacier approximately 2.5 km wide and estimated to be 150 to 180 m deep, serving as a major freshwater source into the fjord.

2.1.1 CTD data

Temperature and salinity data were derived from vertical CTD (RBRconcerto) profiles collected at various locations in the Kong Oscar Fjord system. We focused on data collected in Dickson fjord, and thus considered the downcasts made at locations along the Dickson fjord up to Ella Island, as can be observed in Fig. 1. To conduct measurements close to the glacier terminus, CTD measurements were done using a drone-deployed SonTek CastAway CTD (Poulsen et al. (2022)). This allowed for three CTD casts to be made at distances of around 20, 30, and 50 metres from the glacier terminus, as shown in the flight trajectories in Fig. 1b. Due to constraints of the drone-deployed CTD, these casts do not exceed 100 metres depth.

2.1.2 Stable water isotope data

Stable water isotope samples were collected at five different locations along the Fjord, from 500 m from the glacier front up to Ella Island. The water samples were collected at depths of 1, 5, 10, 20, 30, 50, 75, 100 and 150 m. At stations 1 and 13, additional samples were taken at depths of 200, 210, 220 (station 13), and 250 (station 1) m. The samples were transferred to 2 mL glass vials and remained at room temperature until analysis. The stable hydrogen and oxygen isotope concentrations were determined using a Cavity Ringdown Spectrometer, L2130-i Isotopic sH20 (Picarro Inc., USA). For convenience, the stations have been numbered, with a distinction made between measurements conducted using the drone-deployed CTD (labelled flight 1-3) and the boat-deployed CTD's (station 1-12). The station number increases with the distance from the glacier. The measurements at stations 10 to 12 were conducted on July 31st, the stations 2, 4, 6 and 8 on August 2nd, stations 1, 3, 5, 7, and 9 as well as the drone-deployed casts on August 14th and station 13 on August 15th.

2.1.3 Mooring data

An oceanographic mooring device continuously measuring oceanographic data has been installed just north of Ella Island (Fig. 1). The mooring data is available from August 17th 2022 onwards, and includes oceanographic quantities such as the seawater temperature and salinity, currents, irradiance, fluorescence, and turbidity at the mooring depths of around 30 to 40 m. Alongside this mooring, an on-land observatory measuring atmospheric data such as the air and skin temperature, relative humidity and incoming radiation (Rysgaard et al. (2022b)) is also installed. The combination of these two devices enables simultaneous oceanic and atmospheric measurements.

2.2 Data processing

The Practical Salinity Scale 1978 (PSS-78) was used to compute salinity and depth from the pressure, in-situ temperature, and conductivity measured by the CTDs. For calculation of the potential density, the conservative temperature (temperature insensitive to pressure), the absolute salinity and the specific heat capacity the python implementation of the Gibbs SeaWater
75 (GSW) Oceanographic Toolbox of TEOS-10 package (The TEOS-10 Contributors (2021)) was used. Hydrographic sections of temperature, salinity, density and stable water isotopes were generated with a resolution of 1000 cells in both distance and depth directions. Scientific color maps roma, romaO and hawaii (Crameri (2023)) have been used to prevent visual distortion of the data and to ensure accessibility for readers with color vision deficiencies (Crameri et al. (2020)).

2.2.1 Stable water isotopes

80 To standardise the stable water isotope data measurements, the $\delta^{18}O$ and δ^2H values are expressed relative to the Vienna Standard Mean Ocean Water (VSMOW) as (Geilfus et al. (2023)):

$$\delta^{18}O(‰) = \left[\frac{(^{18}O/^{16}O)_{sample} - (^{18}O/^{16}O)_{VSMOW}}{(^{18}O/^{16}O)_{VSMOW}}\right] \cdot 1000‰ \tag{1}$$

$$\delta^2H(‰) = \left[\frac{(^2H/^1H)_{sample} - (^2H/^1H)_{VSMOW}}{(^2H/^1H)_{VSMOW}}\right] \cdot 1000‰. \tag{2}$$

85 In Greenland, the $\delta^{18}O$ value in glacial water has been measured to be -27.2 $\pm$ 0.2 ‰ (Rysgaard et al. (2024)). To trace the origin of the ocean waters from the isotopic composition, the $\delta^{18}O$ values can be plotted against the δ^2H values. In the resulting diagram, samples of rainwater align along a straight line known as the Meteoric Water Line (MWL), exhibiting a slope of about 8. These line equations are typically of the form $\delta^2H = \pm 8 \cdot \delta^{18}O + d$, where the constant term d is termed the deuterium excess and differs per region (Souchez et al. (2002)). Interestingly, melting and refreezing have been found to decrease the slope of
90 the δ^2H-$\delta^{18}O$ line, though the effect has no uniform effect on the d-excess value (Zhou et al. (2014)). Given that the river water isotopic composition typically correlates well with precipitation composition, the river water isotope values are used to obtain local meteoric water lines (Zhou et al. (2014)). In this study, isotope values will be compared to the Arctic Meteoric Water Line (AMWL), the Global Meteoric Water Line (GMWL), the Lena Meteoric Water Line (LMWL) and the Greenland Ice Sheet (GIS). The $\delta^{18}O$ to δ^2H line equations for the AMWL, LMWL and GMWL are taken from Willcox et al. (2023), and the GIS
95 line equation from Rysgaard et al. (2024).

2.2.2 Water mass partition

To determine the water composition, water mass partitioning can be applied based on different water characteristics. Salinity, temperature, $\delta^{18}O$ and δ^2H are all characteristics that are specific to the different water types and can thus be used for water type identification. In a model brought forward by Washam et al. (2019), adapted by Mortensen et al. (2020), the subglacial
100 freshwater and glacial ice melt partitions are calculated using both the observed salinity and temperature. Since this model

assumes closed conditions, with only ice melting and freshwater inflow affecting water salinity and temperature, the model is not applicable in cases where external processes influence water temperature and salinity. To study whether the temperature increase closer to the terminus is caused by external circumstances or by warm subsurface meltwater mixing, the water masses were separately partitioned based on salinity, temperature, and isotopic composition (δ^{18}O). If the partition of meltwater

105 computed based on the temperature does not correspond to the partition based on the salinity, this heat can not come from warm subsurface freshwater release, and thus must come from external processes.

The following simple temperature-based partition formula has been used to compute the meltwater partition in the water body:

$$f_T = \frac{T_{obs} - T_{WT}}{T_{MW} - T_{WT}}, \tag{3}$$

110 where f_T represents the temperature-based meltwater fraction, T_{obs} the observed temperature, T_{WT} the temperature of the water type at that depth and T_{MW} the meltwater temperature. The same equation has been used for the partitioning based on water salinity and δ^{18}O.

The meltwater temperature and salinity values were taken to be 0 °C and 0, respectively. Since the δ^{18}O values of Polar Water are not depth-dependent, the measured values in the Kong Oscar fjord system for Polar Water (-1.1‰) and glacial

115 meltwater (-27.2‰) are used (Rysgaard et al. (2024)). For the δ^{18}O - based water partitioning calculation, the surface waters were included, as these are going to be used to estimate the ratio of the different meltwater sources. Important to note is that the amount of surface water is likely underestimated, due to sea ice formation resulting in a less depleted signal compared to the meltwater from which it is formed.

3 Results and discussion

120 ### 3.1 Temperature and salinity

The temperature and salinity-depth transects for different stations along the fjord are shown in Fig. 2.
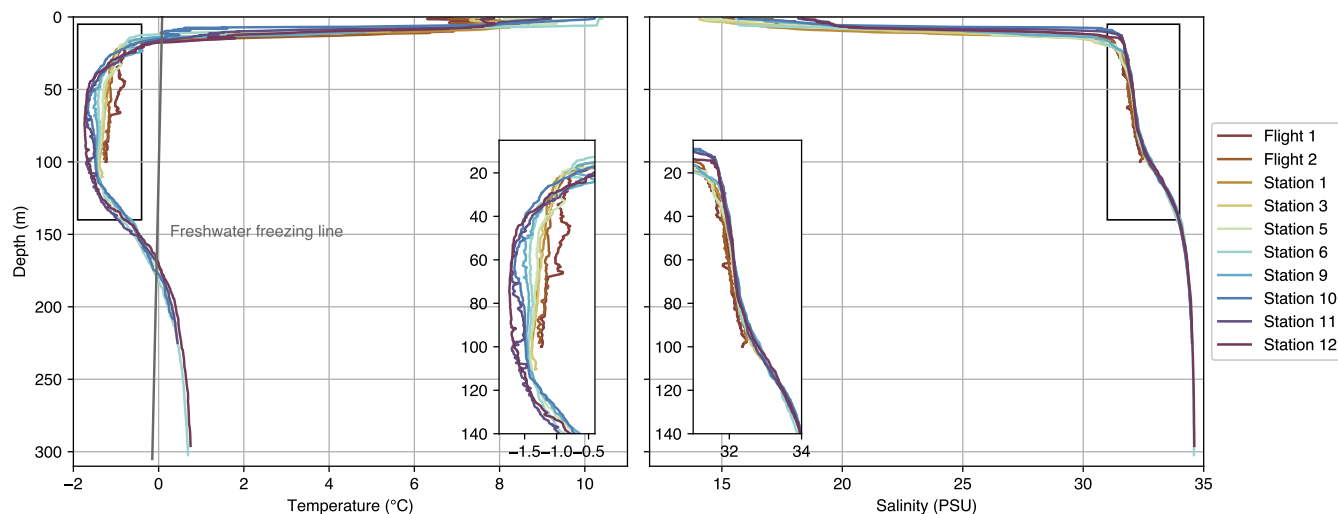
Figure 2. Temperature (left) and salinity (right) variations with depth measured at selected stations across the fjord. Zoomed-in sections are added between 5 and 135 m depth in both plots. In the temperature-depth plot, a pressure-dependent freshwater freezing line is added.

To improve clarity, the plots in Fig. 2 include selected stations chosen based on their significance, showing noteworthy changes or unique characteristics. From these transects, the three distinct water layers typical for East Greenland glacial fjords are distinguishable: the surface water layer (0-20 m depth), the underlying Polar Water layer (20-120 m depth) and the Atlantic Water layer below (Straneo and Cenedese (2015); Rysgaard et al. (2024)). The surface layer is marked by low salinity values due to the freshwater dilution and high temperature caused by atmospheric warming, thus being the lightest layer and stably stratified. The underlying Polar Water layer has low temperatures below the freshwater freezing line ranging from -0.8 to -1.7 °C, depending on the distance and location with respect to the glacier terminus, and corresponding salinity values of around 31.8 to 32.1. The bottom Atlantic Water layer has a relatively stable temperature along the transect, measuring at 0.7 °C at the largest depth measured (300 m), along with characteristically high salinity values measuring at 34.6 at its deepest point, corresponding to Eurasian Basin Atlantic Water (Willcox et al. (2023)). Interestingly, the transects show an increase in temperature in the Polar Water layer closer to the terminus.

Since subaqueous surface melt occurs when ambient seawater is above the pressure-salinity-dependent freezing point, the warm surface waters above the pressure-dependent freezing line (0 to 15 m) and deep Atlantic Waters (from 170 m) could cause surface melt (Fried et al. (2018)). Based on the bathymetric data shown in Fig. 1, which indicates that the fjord terminus does not extend beyond 150 m in depth—thereby limiting its interaction with Atlantic Water—we hypothesise that the primary subsurface melting occurs at the warmer surface water layer, in the upper 20 m.

To further identify and investigate the presence and mixing of various water types, a temperature-salinity (θ-S) plot has been generated in Fig. 3.
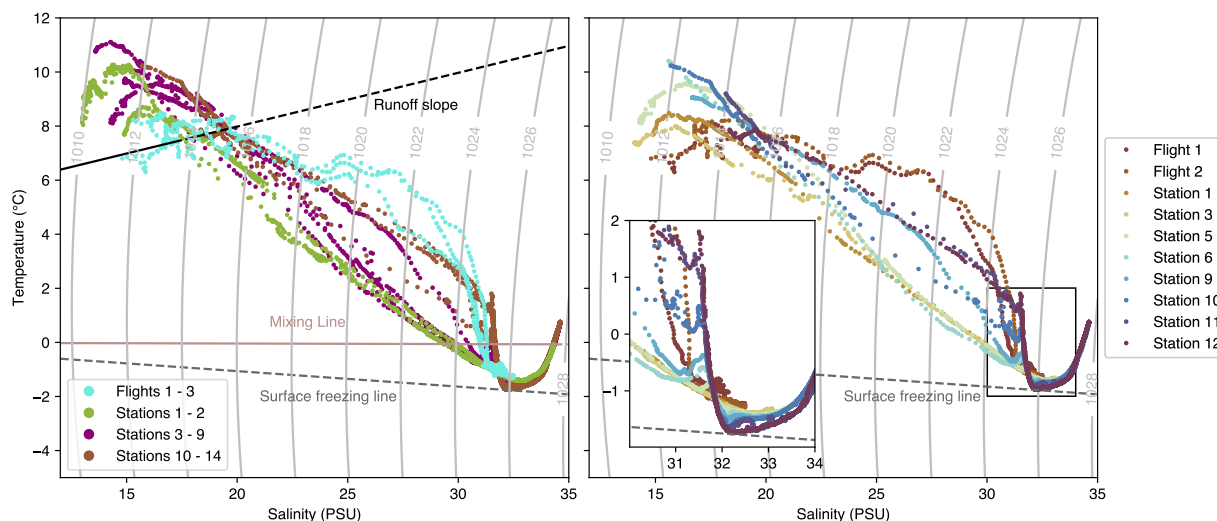
Figure 3. Temperature-salinity values of the transects measured at all the stations clustered (left) and selected stations (right). Both plots include density lines (kg/m^3) and the surface freezing line. The cluster plot includes a runoff slope connecting the surface waters with the glacial runoff and a mixing line connecting deep waters with subglacial discharge.

140   To more easily identify the spatial changes in the water types, clustering was applied based on the measuring location with respect to the terminus. Distinctions were made between the drone-deployed measurements, the deeper measurements relatively close to the glacier terminus (stations 1 and 2), in-fjord measurements up to station 9, and finally the out-fjord measurements up to Ella Island. The θ-S values are relatively variable at salinities of around 31-32 in Fig. 3. Figure 2 shows that this is due to relatively stable Polar Water layer salinity, whilst the temperature changes significantly. Additionally, Fig. 3 again clearly

145 shows the Polar Water becoming colder at a distance further away from the glacier front, with the minimum temperature values (-1.74 °C) measured at station 12 at a salinity of 32 nearly reaching the surface water freezing line values. Furthermore, the gradual mixing of the out-fjord water types with the in-fjord waters seems to occur at salinities around 31.5, with this mixing first detected at station 2. The Flights 1-3 values from the drone-deployed CTD interestingly exhibit colder values at salinities below 18, with the temperature staying relatively constant as the salinity increases up to 26, compared to warmer freshwater

150 becoming colder with salinity at the stations 1 and 2 relatively nearby.

     A runoff slope was plotted in Fig. 3 to investigate runoff mixing. Thermal satellite data showed that surface waters are released with a temperature of approximately 4 °C (Fig. A1, Appendix A). As surface runoff has a salinity of 0, the slope between these values would be a line connecting the surface waters with the point $(\theta, S) = (4 °C, 0)$. To investigate the presence of subglacial discharge in the water body deeper layers, a 'mixing line' was plotted. This represents the line connecting the

155 deeper water body and the subglacial discharge water (Mortensen et al. (2020)). Since subglacial discharge is freshwater at its melting temperature, this water type is characterised by the point $(\theta, S) = (0 °C, 0)$. From the meltwater slope plotted in

Fig. 3, it can be seen that the points do not fall along the mixing line. Therefore, the presence of subglacial discharge in the deeper water body is unlikely. In Flights 1 and 2 data, however, the slope changes from positive to negative in the salinity range 24-28 . This slope becoming positive can be attributed to meltwater influx, as these lines change direction towards the

160   subglacial discharge point $(\theta, S) = (0\ °C, 0)$. Interestingly, in Fig. 3, a slope change occurs in the lower salinity waters, with the lowest salinity water slope parallel to or even steeper than the runoff slope. This phenomenon, indicating freshwater input at the surface, appears up until station 5.

To increase spatial distribution over the observed differences from near the glacier terminus to further out fjord, 2D temperature and salinity sections were generated (Fig. 4). Additionally, a density section was generated to investigate the stability of

165   the water types and identify potential pressure-driven currents.
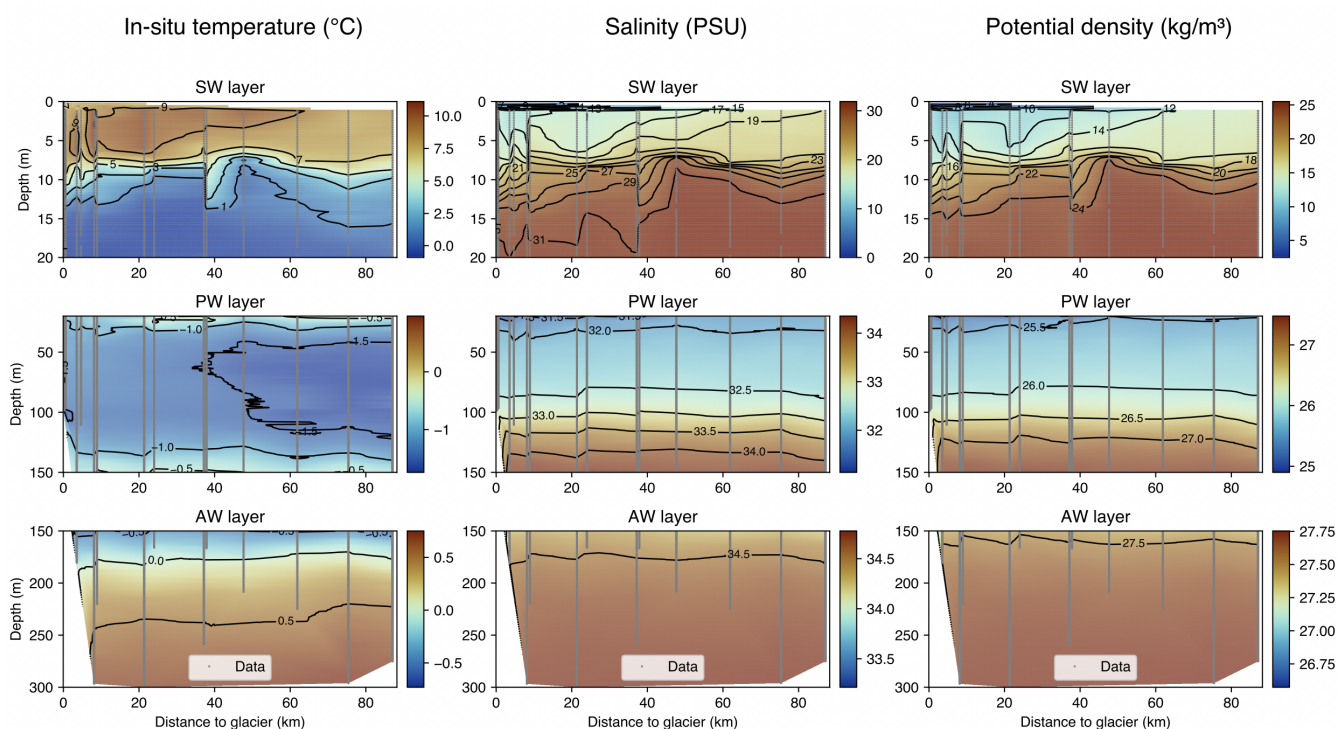
Figure 4. In-situ temperature, practical salinity and potential density sections in the SW, PW and AW layers extending from 20 m to 87 km from the glacier terminus. The grey dots represent the data points of the transects on which the sections are based. Contour lines have been added for every 2 units in the SW layers, and for every 0.5 units in the PW and AW layers.

3.2   Stable water isotopes

To investigate further details in the spatial variation of the stable isotopes along the fjord a contour plot is shown in Fig. 5, along with a plot of $\delta^{18}O$ vs. δ^2H to trace the water origin.
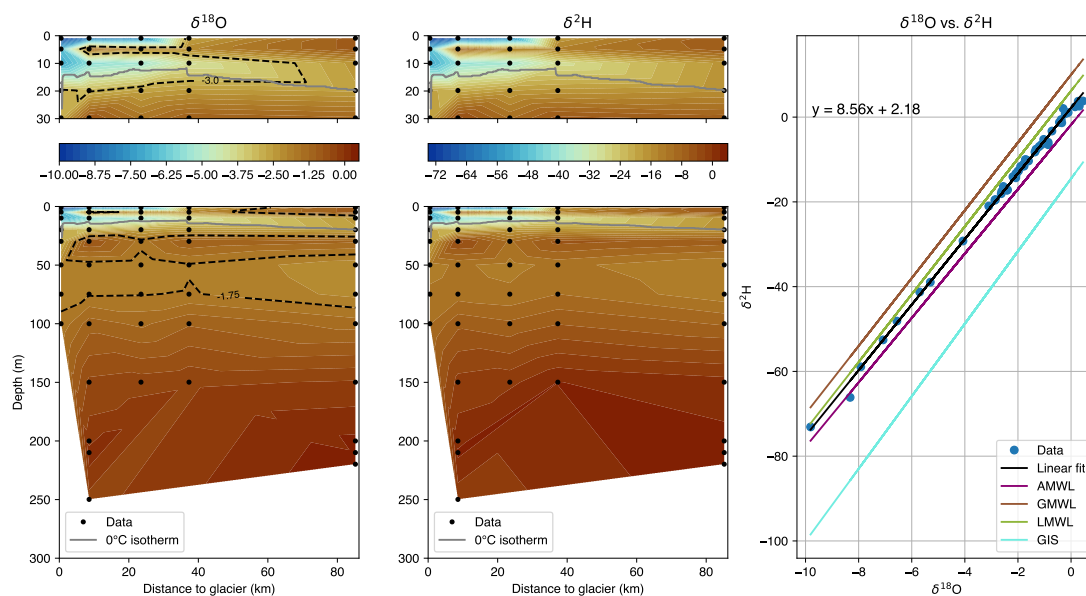
Figure 5. Sections of δ^{18}O and δ^2H extending from 0.5 to 87 km from the glacier terminus, and a plot with the δ^{18}O values plotted against the δ^2H values. All the values are represented in units of ‰. In the contour plots, the black dots represent the transects on which the profiles are based, and the grey line the 0 °C isotherm. Two contours have also been added to the δ^{18}O profile. In the rightmost plot, a black solid line represents the linear fit of the data points, plotted alongside the AMWL, the GMWL, the LMWL (Willcox et al. (2023)) and the GIS line (Rysgaard et al. (2024)).

The δ^{18}O and δ^2H profiles in Fig. 5 illustrate three distinct depleted water signal layers, as highlighted by the contours

170   plotted in the δ^{18}O section. The first is a shallow surface water layer, where the depleted signal extends from the glacier terminus to approximately 35 km, ranging from the surface down to 5 m in depth. Below this surface layer, a second depleted signal is observed, extending from the terminus to 87 km, with the depletion decreasing with distance from the glacier. Notably, there is a sharp separation at the 5 m depth between these two signals, exhibiting less depleted values. The third depleted signal, though less prominent than the surface signals, is found in the Polar Water layer at depths between 50 and 100 m, extending

175   from the terminus to 87 km. Interestingly, this deeper signal becomes more depleted further from the terminus. In the δ^{18}O vs δ^2H plot in Fig. 5, the dataset values fall between the Arctic Meteoric Water Line (AMWL) and the Lena Meteoric Water Line (LMWL). Similarly to the meteoric water lines, the fitted line slope appears to be around 8, with a deuterium excess value (d) of 2.18.

Glacial meltwater sources can be identified by integrating δ^{18}O isotopic data with temperature and salinity data (Hennig

180   et al. (2024)). At a depth of 1 m and up to approximately 35 km from the glacier, high depletion coupled with low salinity has been measured, which is typical of glacial meltwater. This upper surface meltwater signal likely results from glacial runoff and surface melt.

Interestingly, a decrease in the upper surface water depletion has been measured at 5 m depth, shown in Fig. 5. Below this decrease, a second depleted signal was found at around 10 m depth, which no longer would include glacial runoff to the surface

185   ocean, but due to the positive ocean temperatures can still be caused by surface melt (Fried et al. (2018)). Although, for most of the width, the terminus is too shallow to come into contact with the warmer Atlantic Waters to cause surface melt at depth, there is still a depleted water signal distinguishable in the Polar Water layer. While this meltwater signal could be attributed to subglacial discharge, the salinity profile does not show a corresponding freshwater signal.

Notably, the surface water measured beyond 35 km from the terminus, outside Dickson Fjord, is fresh but not isotopically

190   depleted. This surface freshwater may originate from seasonal ice melt (Solomon et al. (2021)). It could derive from the Nordic Seas and Fram Strait, carried by the East Greenland Current (EGC) (de Steur et al. (2009)), or possibly originates within the fjord itself. During the freezing process, heavier isotopes are preferentially incorporated into the ice (fractionation factor of +1.6–2.3‰), resulting in sea-ice meltwater being less isotopically depleted compared to the original seawater (Alkire et al. (2015)). The sharp separation at 5 m depth could then be explained by the inflow of these 'oceanic freshwaters' as the one-

195   ended freshwater release causes a replacement, density-driven, current to flow towards the glacier. Due to the outside surface layer having higher density compared to the surface runoff, the incoming waters will flow below the more buoyant surface waters (classic estuarine circulation driven by the freshwater released at the surface) (Straneo and Cenedese (2015); Rysgaard et al. (2003)). The meltwater discharged at around 10 m, however, will be mixed with waters more saline than the incoming water flow once released. Thus, the incoming water will flow above these heavier waters, creating the observed divide.

200   In the δ^{18}O vs δ^2H plot the fitted line lies between the AMWL and the LMWL. A decrease in d-excess value could be attributed to contributions from the GIS, since the d-excess for the GIS line is much smaller compared to the relevant meteoric water lines shown. An interesting observation from Rysgaard et al. (2024) isotopic analysis is that measurements taken in the out-fjord region of Northeast Greenland exhibit a closer alignment with the LMWL. This suggests a more substantial contribution from the Greenland ice-sheet closer to the glacier. Further, the slope of the fitted line seems to be slightly less

205   steep compared to the meteoric water lines, which could be the result of meltwater contribution to the water body, as described in section 2.2.1.

3.3   Water mass partitioning

The meltwater partition profiles based on water type salinity, temperature and δ^{18}O, respectively, are presented in Fig. 6.
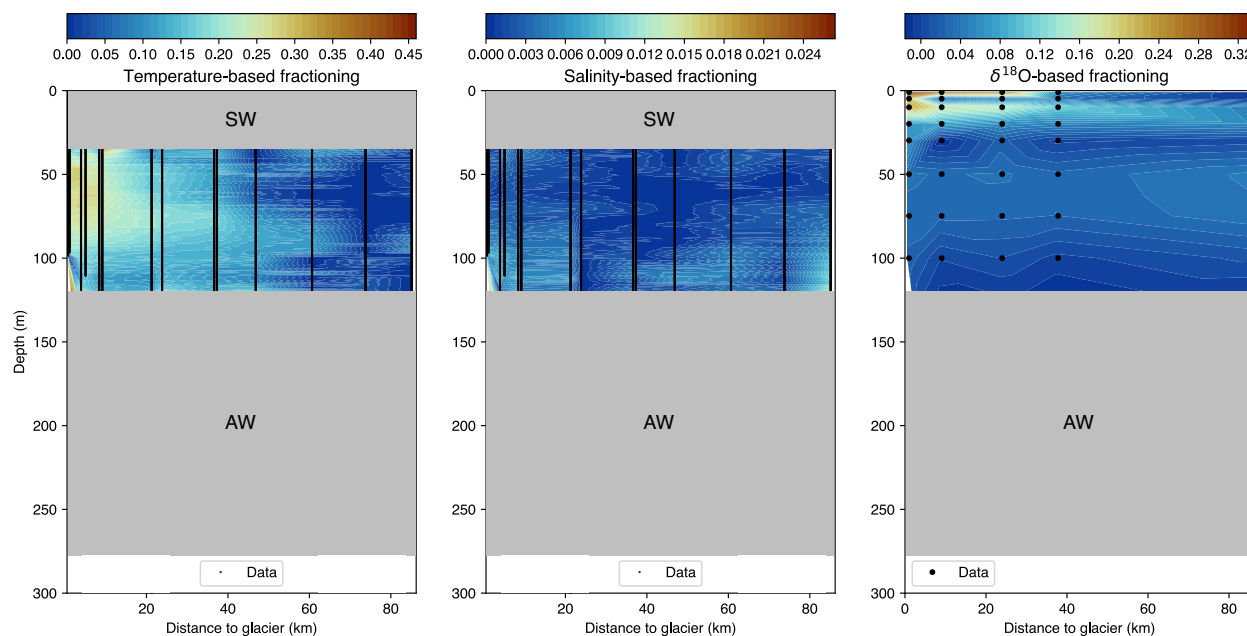
Figure 6. Graph depicting the Polar Water layer meltwater partition based on water temperature, salinity and δ^{18}O, respectively. The black dots represent the data points which have been used to create the profile grid values used in the meltwater partition calculation. The surface water (SW) and Atlantic Water (AW) layers are not considered in the temperature and salinity-based partitioning calculation and are thus covered by grey blocks. In the δ^{18}O partitioning, only Atlantic Waters have been excluded from the partitioning.

In Fig. 6 there is a large discrepancy between the temperature and salinity-based partition values, with the temperature-based partition values significantly larger than the salinity-based partitions. This confirms that the excess heat in the Polar Water body does not come from the liquid warmer glacial meltwater. Using the salinity-based meltwater partition values, the corresponding freshwater contribution to the temperature in the water body was computed. This contribution was then subtracted from the observed temperature profile to calculate the excess heat required to reach the measured temperatures. This heat was obtained through element-wise multiplication of the excess temperature matrix with the specific heat capacity and density matrices. After applying a 2D Riemann sum to the resulting matrix and multiplying this value with the estimated average fjord width, 3 km, an excess Polar Water layer heat estimate of $1.1 \cdot 10^{16}$ J was found in Dickson fjord (up to station 9). The discrepancy between the Polar Water layer salinity-based and δ^{18}O-based partitioning can be explained by the salinity values being compared to the minimum value at each depth, rather than an absolute value since the salinity can also be changed by freshwater sources that are not subglacial meltwater. Thus, these values are taking the mixing and transition of the various water bodies into account, whereas with the δ^{18}O-based partitioning this was not necessary. The only contribution to the δ^{18}O depletion is glacial meltwater, freezing processes and precipitation, making it safe to assume a constant δ^{18}O Polar Water value

along the different depths, but having a higher partitioning of meltwater in the Polar Water layer as a result (since the spatial variance of salinity and δ^{18}O in only the Polar Water layer is not as high, comparatively).

Since the Dickson fjord width remains relatively constant, the δ^{18}O profile can be used to roughly estimate the meltwater
225 ratio in the fjord. The ratio of surface meltwater (SMW), subsurface meltwater (SSMW), and Polar Water layer meltwater (PLMW) was estimated to be 22%:31%:47%. However, the surface meltwater partition is underestimated because the effect of sea ice formation, which decreases δ^{18}O depletion, was not accounted for in the calculations.

3.4 Frazil ice crystal formation

Bathymetry measurements show that the terminus is exclusively in contact with the surface waters and cold Polar Waters.
230 Since the seawater temperatures in the Polar Water layer are below freshwater freezing temperature, as can be seen in Fig. 2, we hypothesise that the meltwater refreezes once it is released at depth. Frazil ice crystals are then formed because of this freezing process, releasing latent heat to the ambient water. These ice crystals then slowly float to the surface due to their buoyancy (Dmitrenko et al. (2010)), melting once they reach freshwater melting temperatures at the surface, releasing freshwater into the fjord. A schematic of this process is displayed in Fig. 7a.

235 A similar refreezing effect was observed by Marchenko et al. (2017) near the glacier front of Paula Glacier in Spitsbergen. In this paper, the authors also attribute the refreezing to meltwater mixing with seawater below the freshwater freezing point, leading to the formation of frazil ice crystals. A comparable process of platelet ice crystal formation has been described by Hoppmann et al. (2020), with a difference being that in our case, the primary freshwater source is surface freshwater released at depth, rather than basal melt.

240 This process could explain the excess heat in the Polar Water layer, as this may result from latent heat released by meltwater refreezing at depth. Additionally, the melting of ice crystals in the surface water layer would explain the freshwater input observed in the surface waters away from the terminus (up to station 5) in Fig. 3. For the frazil ice crystal formation to account for the excess heat estimate in the Polar Water layer, the total volume of meltwater to be refrozen amounts to $3.37 \cdot 10^7$ m^3, assuming a stagnant water body. Along with the excess heat, this refreezing process would also clarify the subsurface depleted
245 δ^{18}O signal in Fig. 5, which indeed occurs around the freshwater freezing line, where the ice crystals would melt, and the glacial freshwater released. To fully explain the excess heat estimated in the fjord through the latent heat released, the quantity of water required to be refrozen equals $3.4 \cdot 10^7$ m^3. Comparing this amount to the meltwater release estimates by Karlsson et al. (2023) this value seems to be close to the surface meltwater estimate of $3.6 \cdot 10^7$ m^3 in August 2022.

However, while this hypothesis aligns with the low Polar Water temperatures and could explain the excess heat observed in
250 the isotopic profiles, more research is required to validate the presence of frazil ice crystals in the Polar Water body. In-situ observation of these crystals is crucial for this validation, although obtaining these observations is challenging (Hoppmann et al. (2020)). We attempted to film these crystals with an Autonomous Underwater Vehicle (AUV) and observed numerous particles near the glacier, while turbidity values remained low. We anticipate these particles to be frazil ice crystals. This aspect of our work will be detailed and published elsewhere.

3.5 Heat budget

A heat budget estimate was made to assess the different heat sources in Dickson fjord. A similar approach was used by Bendtsen et al. (2015), where the authors conducted energy budget calculations for Kangersuneq. Assuming that the Atlantic Water layer has limited interaction with the glacier front and minimal heat exchange with the water bodies above, since the terminus does not reach Atlantic Water layer depths, this layer was excluded from the heat budget calculations . Nevertheless, its total heat content was estimated to highlight the substantial thermal energy stored within. This stored heat could become relevant during significant events such as substantial calving, potentially causing interactions between this layer and the overlaying water. Consequently, for our heat budget calculations, the surface area of the fjord is approximated as 116 km^2, with an average depth of approximately 200 m, amounting to a total volume of around 23.2 km^3.

For the heat balance estimates, the meltwater flux estimates by Karlsson et al. (2023) were used. They combined different data sets to give an estimate of the solid-ice discharge, surface, and basal melt of the Hisinger glacier for the month of August every year between 2010 and 2020. Since August 2022 basal and surface melt have not been assessed yet, and these values do not seem to vary too much between years, the 2010-2020 August averages of these quantities were used for computations. These equal $3.6 \cdot 10^7$ m^3 for surface melt and $2.6 \cdot 10^6$ m^3 for basal melt. Important to note is that the surface melt values also represent the surface meltwater that is discharged at depth through glacial channels. Once the volume flux into the fjord is known, the following equation was used to compute the heat flux q:

$$q = \rho c_p Q \Delta\theta, \tag{4}$$

with $\Delta\theta$ the difference between the water temperature of the in- or outflowing water and the ambient water, Q the volume flux and ρ and c_p the temperature, salinity, density and specific heat capacity of the in-or outflowing water, respectively.

The heat sources taken into account in this heat budget are; the atmospheric heat (radiative, latent and sensible heat), the heat loss into melting solid ice discharge, the heat from surface runoff subglacial discharge and basal melt, and the potential latent heat from frazil ice crystal formation.

Through mooring, the 24-hour averaged net incoming radiation measured at Ella Island from the 21st to the 31st of August 2022 was obtained, which equals 123.4 W/m^2. Additionally, a mean August Atlantic Ocean albedo at 70 °N (Payne (1972)) of 0.09 was found. Assuming minimal ice coverage in Dickson Fjord, this value is used for the energy influx calculation, resulting in an energy influx from radiation of approximately 13.0 GW. Since quantities relevant for the latent and sensible heat, such as wind speed, relative humidity, and temperature, are very similar between Zackenberg (mooring located at Northeast Greenland 74 °N) and Ella Island observatories in August 2022, the average latent and sensible heat fluxes measured in Zackenberg in August 2022 were used for the atmospheric heat estimate (Rysgaard et al. (2022a)). From the Zackenberg measurement station, we obtain an August average latent heat flux of 25.6 W/m^2 and a sensible heat flux of 61.5 W/m^2, measured at 2.5 m height near the fjord water. The total sensible and latent heat fluxes over the area of 116km^2 amount to 7.1 GW and 3.0 GW. Important to note is that these values are not an exact representation of the actual latent and sensible heat fluxes, since they were not measured right above the water. Subtracting these values from the incoming radiative heat flux, the total atmospheric heat contribution was estimated atas 2.9 GW. The energy that goes into melting glacial icebergs was computed using iceberg calving estimates,

since this ice will be melted by the warm surface waters. According to computations by Karlsson et al. (2023), $3.64 \cdot 10^6$ m^3 of

290   ice calved off in August 2022. Assuming all this ice melts and using a latent heat of fusion of approximately $3.34 \cdot 10^8$ J/m^3, the heat rate going towards iceberg melting amounts to approximately 0.45 GW. As surface melt estimates can be released in two ways, as surface runoff and subglacial discharge, the heat impact of this meltwater varies based on its discharge location. Due to this variability, a range of estimates was computed for the heat contributions of these meltwaters. To obtain this range, the heat contribution was computed for two scenarios: one where all surface melt is discharged at the surface (where ambient

295   water temperatures are higher, resulting in a negative heat flux), and another where all meltwater is discharged at the coldest part of the Polar Water layer (resulting in a maximum heat contribution from this meltwater). For the first scenario, assuming all $3.6 \cdot 10^7$ m^3 is discharged at the surface and a $\Delta\theta$ of 2 °C, a total heat flux of -0.11 GW in August 2022 was obtained using Eq. 6. For the second scenario, assuming the meltwater discharged is around 0 °C, a specific heat capacity and density of respectively 4215 J/(kg·K) and 1000 kg/m^3 was found, amounting to a total heat flux of around 0.08 GW in August 2022.

300   Therefore, the heat flux due to glacial meltwater release in August 2022 was estimated to be in the range of -0.11 GW - 0.08 GW. Assuming the main fjord water exchange is driven by estuarine circulation, the volume fluxes were estimated through the Knudsen theorem for estuarine exchange flow (Burchard et al. (2018)). After obtaining the volume flux of the layer at the fjord's end, station 9, Eq. 6 was used to determine the heat flux out of the fjord. For the first scenario, all the surface melt was assumed to discharge in the upper layer and the basal melt estimate was taken as the lower layer inflow. For the

305   second scenario, both the surface melt and basal melt were taken as the lower layer inflow. Temperature differences between measurements taken at station 9 and those at Ella Island were taken as 0.5 °C in the upper layer and 0.2 °C in the lower layer. This resulted in a heat outflow estimate of 0.036 GW for the first scenario and 0.0148 GW for the second scenario. Since it remains unknown whether the frazil ice crystal formation occurs, as well as the quantity of ice crystals that are present in the water body, only a potential energy range can be estimated. For the upper limit, the sum of the surface and basal meltwater

310   estimates was used, which equals $3.86 \cdot 10^7$ m^3. Assuming that all these crystals remain frozen and a latent heat of $3.34 \cdot 10^8$ J/m^3, this amounts to a maximum heat flux of 4.8 GW in August 2022. It is crucial to note that if the meltwater refreezes, the liquid state no longer contributes to the heat budget. Consequently, the values for surface runoff and subglacial discharge are tied to the latent heat values. The average in-fjord depth of the water body was taken as 450 m, therefore estimating the total Atlantic Water volume to be 29 km^3. Figure 2 shows a salinity of 34.6 and temperature value of 0.7 °C in the Atlantic Water

315   layer at 300 m depth. Using these values, a specific heat capacity and density of 3979 J/(kg·K) and 1029 kg/m^3 was found, resulting in a heat content of approximately $8.3 \cdot 10^7$ GJ.

In Fig. 7b, a schematic illustrates the combined heat contribution estimated in this section. While this offers an initial understanding of the heat sources and their magnitudes, it's crucial to acknowledge the numerous assumptions and estimates embedded in the calculations. Nevertheless, the heat budget estimate indicates that, apart from the latent heat release attributed

320   to potential meltwater refreezing, there does not appear to be a heat source contributing to the temperature rise within the Polar Water layer. Comparing our findings to those of Bendtsen et al. (2015), we observe that our heat source estimates are significantly smaller. This is likely due to the much smaller surface area in our Dickson Fjord calculations (116 km^2 in Dickson

vs. 400 km^2 in Kangersuneq). Additionally, the glacier in the Kangersuneq area appears to be more active, thus adding and extracting more heat to the fjord.
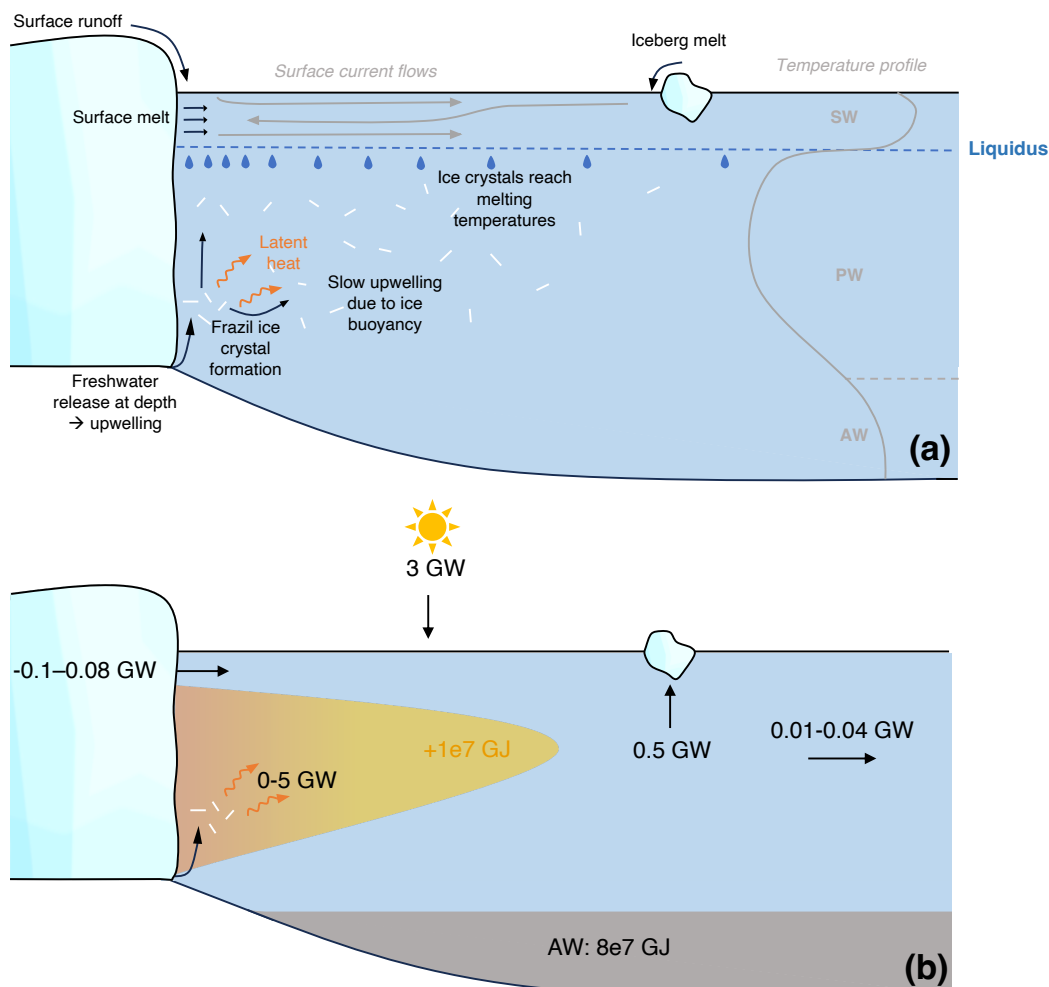
Figure 7. (a) Schematic picture of our interpretation of the data depicting glacial meltwater refreezing and frazil ice crystal formation in the Polar Water layer. The grey arrows represent the theorised surface water currents as a result of both surface melting and runoff. A sketch of a typical measured temperature profile with the water types is included in grey. (b) Schematic depicting the heat budget estimates for Dickson Fjord in August 2022. The grey arrows represent the upper (surface water) and lower (Polar water) layer estimates of the outflowing heat flux. The orange-yellow gradient represents the excess heat estimated in the Polar Water layer. The bottom grey water body represents the heat stored in the Atlantic Water layer.

4 Conclusions

This study aimed to understand the complex ice-ocean processes within Dickson Fjord during peak summer melt conditions (August 2022). By combining hydrographic and stable isotope observations at various depths and locations, we investigated the fate of subglacial meltwater in a fjord dominated by cold Polar Water.

Bathymetry measurements showed that the terminus is exclusively in contact with surface waters and cold Polar Waters. Since the seawater temperatures in the Polar Water layer are below the freshwater freezing point, as shown in Fig. 2, we hypothesise that meltwater refreezes once it is released at depth. This refreezing process leads to the formation of frazil ice crystals, which release latent heat to the surrounding water. These ice crystals slowly float to the surface due to their buoyancy and melt once they reach freshwater melting temperatures, releasing freshwater into the fjord. This process is illustrated in Fig. 7a and is similar to the platelet ice crystal formation described by Hoppmann et al. (2020), with the key difference being that in our case, the primary freshwater source is surface freshwater released at depth rather than basal melt. The temperature and salinity data revealed a three-layer stably stratified water body: a fresh, warm surface layer; an underlying cold Polar Water layer; and a warm, saline Atlantic Water layer at the bottom. The glacier terminus was primarily in contact with cold Polar Waters near the freezing point, with an increase in Polar Water layer temperature closer to the terminus. Water fraction calculations indicated that this heat increase could not be solely due to liquid meltwater release, with an unaccounted heat estimated at $1.1 \cdot 10^{16}$ J. Isotope partitioning suggested an in-fjord meltwater distribution of 22% surface meltwater, 31% subsurface meltwater, and 47% Polar Water layer meltwater, though this likely underestimates surface meltwater due to unaccounted sea-ice formation.

The process of meltwater refreezing at depth would explain the excess heat present in the Polar Water layer, attributed to latent heat release. To account for the excess heat estimate in the Polar Water layer through frazil ice crystal formation, the total volume of meltwater required to refreeze amounts to $3.37 \cdot 10^7$ m^3, assuming a stagnant water body. This refreezing process also clarifies the subsurface depleted d^{18}O signal in Fig. 5, occurring around the freshwater freezing line where ice crystals melt and release glacial freshwater. To fully explain the excess heat estimated in the fjord, the quantity of water required to refreeze is $3.4 \cdot 10^7$ m^3. Comparing this amount to the meltwater release estimates by Karlsson et al. (2023), this value is close to the surface meltwater estimate of $3.6 \cdot 10^7$ m^3 in August 2022. While this hypothesis aligns with low Polar Water temperatures and could explain the excess heat observed in the isotopic profiles, more research is required to validate the presence of frazil ice crystals in the Polar Water body. In-situ observation of these crystals is crucial for validation, although obtaining these observations is challenging.

Further studies are needed to provide more precise estimates of subsurface freshwater inflow and fjord outflow, to determine if the Polar Water layer heat increase can indeed be explained by meltwater refreezing (frazil ice formation). Simulations of freshwater release into saline waters and detailed fjord system models could enhance our understanding of fjord heat budgets and current flows. Additionally, research focusing on in-fjord currents, especially in- and outflows at different depths, could offer valuable insights into the fjord's heat content and dynamics. Continuous isotopic water sampling across various depths and locations would help identify the movement and outflow patterns of glacial meltwater. In conclusion, this study sheds

light on the freshwater dynamics and glacier-ocean interactions within Dickson Fjord during peak summer melt conditions.
360 The observed phenomena of frazil ice formation and unresolved questions underscore the need for further research to fully understand the complexities of glacial meltwater behaviour.

Data availability. Data is currently under submission in the Pangaea data repository.

Appendix A: Thermal image Dickson Fjord
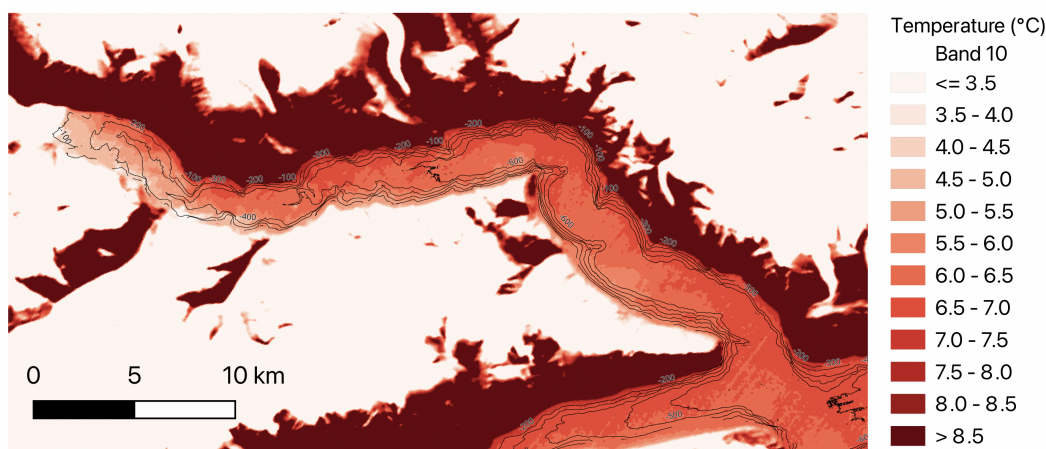
Figure A1. Thermal image of Dickson Fjord, including high-resolution 100 m bathymetry contour lines. The thermal image was generated using satellite data from the Landsat 8 OLI/TIRS satellite (Band 10) on the 20th of August 2022.

Author contributions. Conceptualization: S. Rysgaard and F. Rooijakkers. Data analysis: All. Investigation: E. Poulsen and S. Rysgaard.
365 Project administration: S. Rysgaard. Visualization: F. Rooijakkers. Writing original draft: F. Rooijakkers. Writing, review and editing: All.

Competing interests. No competing interests are present.

Acknowledgements. AI tools have been used to check and improve spelling and grammar.

References

Alkire, M. B., Nilsen, F., Falck, E., Søreide, J., and Gabrielsen, T. M.: Tracing sources of freshwater contributions to first-year sea ice in
Svalbard fjords, Continental Shelf Research, 101, 85–97, https://doi.org/https://doi.org/10.1016/j.csr.2015.04.003, 2015.

Arndt, J. E., Jokat, W., Dorschel, B., Myklebust, R., Dowdeswell, J. A., and Evans, J.: A new bathymetry of the Northeast
Greenland continental shelf: Constraints on glacial and other processes, Geochemistry, Geophysics, Geosystems, 16, 3733–3753,
https://doi.org/https://doi.org/10.1002/2015GC005931, 2015.

Bendtsen, J., Mortensen, J., and Rysgaard, S.: Modelling subglacial discharge and its influence on ocean heat transport in Arctic fjords,
Ocean Dynamics, 65, 1535–1546, https://doi.org/10.1007/s10236-015-0883-1, 2015.

Burchard, H., Bolding, K., Feistel, R., Gräwe, U., Klingbeil, K., MacCready, P., Mohrholz, V., Umlauf, L., and van der Lee, E. M.: The
Knudsen theorem and the Total Exchange Flow analysis framework applied to the Baltic Sea, Progress in Oceanography, 165, 268–286,
https://doi.org/https://doi.org/10.1016/j.pocean.2018.04.004, 2018.

Crameri, F.: Scientific colour maps, https://doi.org/10.5281/zenodo.8409685, 2023.

Crameri, F., Shephard, G. E., and Heron, P. J.: The misuse of colour in science communication, Nature Communications, 11, 5444,
https://doi.org/10.1038/s41467-020-19160-7, 2020.

de Steur, L., Hansen, E., Gerdes, R., Karcher, M., Fahrbach, E., and Holfort, J.: Freshwater fluxes in the East Greenland Current: A decade
of observations, Geophysical Research Letters, 36, https://doi.org/https://doi.org/10.1029/2009GL041278, 2009.

Dmitrenko, I. A., Wegner, C., Kassens, H., Kirillov, S. A., Krumpen, T., Heinemann, G., Helbig, A., Schröder, D., Hölemann, J. A., Klagge,
T., Tyshko, K. P., and Busche, T.: Observations of supercooling and frazil ice formation in the Laptev Sea coastal polynya, Journal of
Geophysical Research: Oceans, 115, https://doi.org/https://doi.org/10.1029/2009JC005798, 2010.

Fried, M. J., Catania, G. A., Stearns, L. A., Sutherland, D. A., Bartholomaus, T. C., Shroyer, E., and Nash, J.: Reconciling Drivers of Seasonal
Terminus Advance and Retreat at 13 Central West Greenland Tidewater Glaciers, Journal of Geophysical Research: Earth Surface, 123,
1590–1607, https://doi.org/https://doi.org/10.1029/2018JF004628, 2018.

Geilfus, N.-X., Delille, B., Tison, J.-L., Lemes, M., and Rysgaard, S.: Gas dynamics within landfast sea ice of an Arctic fjord (NE Greenland)
during the spring–summer transition, Elementa: Science of the Anthropocene, 11, 00 056, https://doi.org/10.1525/elementa.2022.00056,
2023.

Hennig, A. N., Mucciarone, D. A., Jacobs, S. S., Mortlock, R. A., and Dunbar, R. B.: Meteoric water and glacial melt in the southeastern
Amundsen Sea: a time series from 1994 to 2020, The Cryosphere, 18, 791–818, https://doi.org/10.5194/tc-18-791-2024, 2024.

Holland, P., Jenkins, A., and Holland, D.: The response of Ice shelf basal melting to variations in ocean temperature, Journal of Climate, 21,
2558–2572, https://doi.org/10.1175/2007JCLI1909.1, 2008.

Hoppmann, M., Richter, M. E., Smith, I. J., Jendersie, S., Langhorne, P. J., Thomas, D. N., and Dieckmann, G. S.: Platelet ice, the Southern
Ocean's hidden ice: a review, Annals of Glaciology, 61, 341–368, https://doi.org/10.1017/aog.2020.54, 2020.

Karlsson, N. B., Mankoff, K. D., Solgaard, A. M., Larsen, S. H., How, P. R., Fausto, R. S., and Sørensen, L. S.: A data set of monthly
freshwater fluxes from the Greenland ice sheet's marine-terminating glaciers on a glacier–basin scale 2010–2020, GEUS Bulletin, 53,
https://doi.org/10.34194/geusb.v53.8338, 2023.

Khan, S. A., Kjær, K. H., Bevis, M., Bamber, J. L., Wahr, J., Kjeldsen, K. K., Bjørk, A. A., Korsgaard, N. J., Stearns, L. A., van den Broeke,
M. R., Liu, L., Larsen, N. K., and Muresan, I. S.: Sustained mass loss of the northeast Greenland ice sheet triggered by regional warming,
Nature Climate Change, 4, 292–299, https://doi.org/10.1038/nclimate2161, 2014.

405   Marchenko, A., Morozov, E., and Marchenko, N.: Supercooling of seawater near the glacier front in a fjord, Earth Science Research, 6, 97–108, 2017.

Mortensen, J., Rysgaard, S., Bendtsen, J., Lennert, K., Kanzow, T., Lund, H., and Meire, L.: Subglacial Discharge and Its Down-Fjord Transformation in West Greenland Fjords With an Ice Mélange, Journal of Geophysical Research: Oceans, 125, e2020JC016301, https://doi.org/https://doi.org/10.1029/2020JC016301, e2020JC016301 2020JC016301, 2020.

410   Payne, R. E.: Albedo of the Sea Surface, Journal of Atmospheric Sciences, 29, 959 – 970, https://doi.org/https://doi.org/10.1175/1520-0469(1972)029<0959:AOTSS>2.0.CO;2, 1972.

Poulsen, E., Eggertsen, M., Jepsen, E. H., Melvad, C., and Rysgaard, S.: Lightweight drone-deployed autonomous ocean profiler for repeated measurements in hazardous areas – Example from glacier fronts in NE Greenland, HardwareX, 11, e00313, https://doi.org/https://doi.org/10.1016/j.ohx.2022.e00313, 2022.

415   Rysgaard, S., Vang, T., Stjernholm, M., Rasmussen, B., Windelin, A., and Kiilsholm, S.: Physical Conditions, Carbon Transport, and Climate Change Impacts in a Northeast Greenland Fjord, Arctic, Antarctic, and Alpine Research, 35, 301–312, https://doi.org/10.1657/1523-0430(2003)035[0301:PCCTAC]2.0.CO;2, 2003.

Rysgaard, S., Bjerge, K., Boone, W., Frandsen, E., Graversen, M., Thomas Høye, T., Jensen, B., Johnen, G., Antoni Jackowicz-Korczynski, M., Taylor Kerby, J., Kortegaard, S., Mastepanov, M., Melvad, C., Schmidt Mikkelsen, P., Mortensen, K., Nørgaard, C.,
420   Poulsen, E., Riis, T., Sørensen, L., and Røjle Christensen, T.: A mobile observatory powered by sun and wind for near real time measurements of atmospheric, glacial, terrestrial, limnic and coastal oceanic conditions in remote off-grid areas, HardwareX, 12, https://doi.org/10.1016/j.ohx.2022.e00331, 2022a.

Rysgaard, S., Bjerge, K., Boone, W., Frandsen, E., Graversen, M., Thomas Høye, T., Jensen, B., Johnen, G., Antoni Jackowicz-Korczynski, M., Taylor Kerby, J., Kortegaard, S., Mastepanov, M., Melvad, C., Schmidt Mikkelsen, P., Mortensen, K., Nørgaard, C., Poulsen,
425   E., Riis, T., Sørensen, L., and Røjle Christensen, T.: A mobile observatory powered by sun and wind for near real time measurements of atmospheric, glacial, terrestrial, limnic and coastal oceanic conditions in remote off-grid areas, HardwareX, 12, e00331, https://doi.org/https://doi.org/10.1016/j.ohx.2022.e00331, 2022b.

Rysgaard, S., Mortensen, J., Haxen, M., Gillard, L. C., and Risgaard-Petersen, N.: Summer Hydrography Conditions at Proglacial Fjord Entrances Along East Greenland, Journal of Geophysical Research: Oceans, 129, e2023JC020665,
430   https://doi.org/https://doi.org/10.1029/2023JC020665, e2023JC020665 2023JC020665, 2024.

Solomon, A., Heuzé, C., Rabe, B., Bacon, S., Bertino, L., Heimbach, P., Inoue, J., Iovino, D., Mottram, R., Zhang, X., Aksenov, Y., McAdam, R., Nguyen, A., Raj, R. P., and Tang, H.: Freshwater in the Arctic Ocean 2010–2019, Ocean Science, 17, 1081–1102, https://doi.org/10.5194/os-17-1081-2021, 2021.

Souchez, R., Lorrain, R., and Tison, J.-L.: Stable water isotopes and the physical environment, Belgeo, 2,
435   https://doi.org/10.4000/belgeo.16199, 2002.

Straneo, F. and Cenedese, C.: The Dynamics of Greenland's Glacial Fjords and Their Role in Climate, Annual Review of Marine Science, 7, 89–112, https://doi.org/10.1146/annurev-marine-010213-135133, pMID: 25149564, 2015.

Straneo, F., Sutherland, D. A., Holland, D., Gladish, C., Hamilton, G. S., Johnson, H. L., Rignot, E., Xu, Y., and Koppes, M.: Characteristics of ocean waters reaching Greenland's glaciers, Annals of Glaciology, 53, 202–210, https://doi.org/10.3189/2012AoG60A059, 2012.

440   The TEOS-10 Contributors: gsw package for Python, https://github.com/TEOS-10/GSW-Python, 2021.

Velicogna, I.: Increasing rates of ice mass loss from the Greenland and Antarctic ice sheets revealed by GRACE, Geophysical Research Letters, 36, https://doi.org/https://doi.org/10.1029/2009GL040222, 2009.

Washam, P., Nicholls, K. W., Münchow, A., and Padman, L.: Summer surface melt thins Petermann Gletscher Ice Shelf by enhancing channelized basal melt, Journal of Glaciology, 65, 662–674, https://doi.org/10.1017/jog.2019.43, 2019.

445 Willcox, E. W., Bendtsen, J., Mortensen, J., Mohn, C., Lemes, M., Juul-Pedersen, T., Holding, J., Møller, E. F., Sejr, M. K., Seidenkrantz, M.-S., and Rysgaard, S.: An Updated View of the Water Masses on the Northeast Greenland Shelf and Their Link to the Laptev Sea and Lena River, Journal of Geophysical Research: Oceans, 128, e2022JC019 052, https://doi.org/https://doi.org/10.1029/2022JC019052, e2022JC019052 2022JC019052, 2023.

Zhao, K.: Standing Eddies in Glacial Fjords and their Role in Fjord Circulation and Melt, https://doi.org/10.1002/essoar.10511100.1, 2022.

450 Zhou, S., Wang, Z., and Joswiak, D. R.: From precipitation to runoff: stable isotopic fractionation effect of glacier melting on a catchment scale, Hydrological Processes, 28, 3341–3349, https://doi.org/https://doi.org/10.1002/hyp.9911, 2014.